Supplementary Material

Depth-dependent sulfur speciation in modern carbonate microbialites from a monomictic lake

Caumartin, J., Benzerara, K., Havas, R., Thomazo, C., Mehta, N., Betancourt, V., Colocho Hurtarte, L. C., Cotte, M., Estève, I., Jézéquel, D., Kotopoulou, E., Sans-Jofre, P., Tavera, R., & López-García P.

(2026). *Advances in Geochemistry and Cosmochemistry*, *2*(1), 988.

https://doi.org/10.33063/agc.v2i1.988

Supplementary Figures

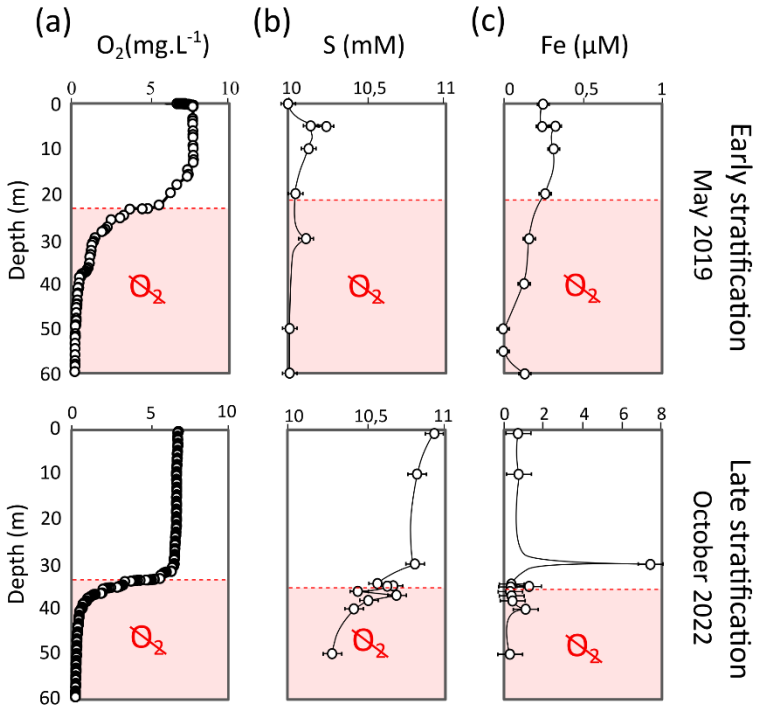

Figure S1: *Depth profiles of the (a) dissolved oxygen (in mg.L^{-1}; precision at 0.1 mg.L^{-1}), (b) S (in mM; precision at 5%) and (c) iron (in mM at 5%) concentrations in the Lake Alchichica water column. On the top line: profiles during early stratification in May 2019; on the bottom line: profile during late stratification in October 2022. The anoxic bottom layer of the water is colored in red and the measured oxycline was slightly deeper in the late stratification period in 2022 than in 2019.*

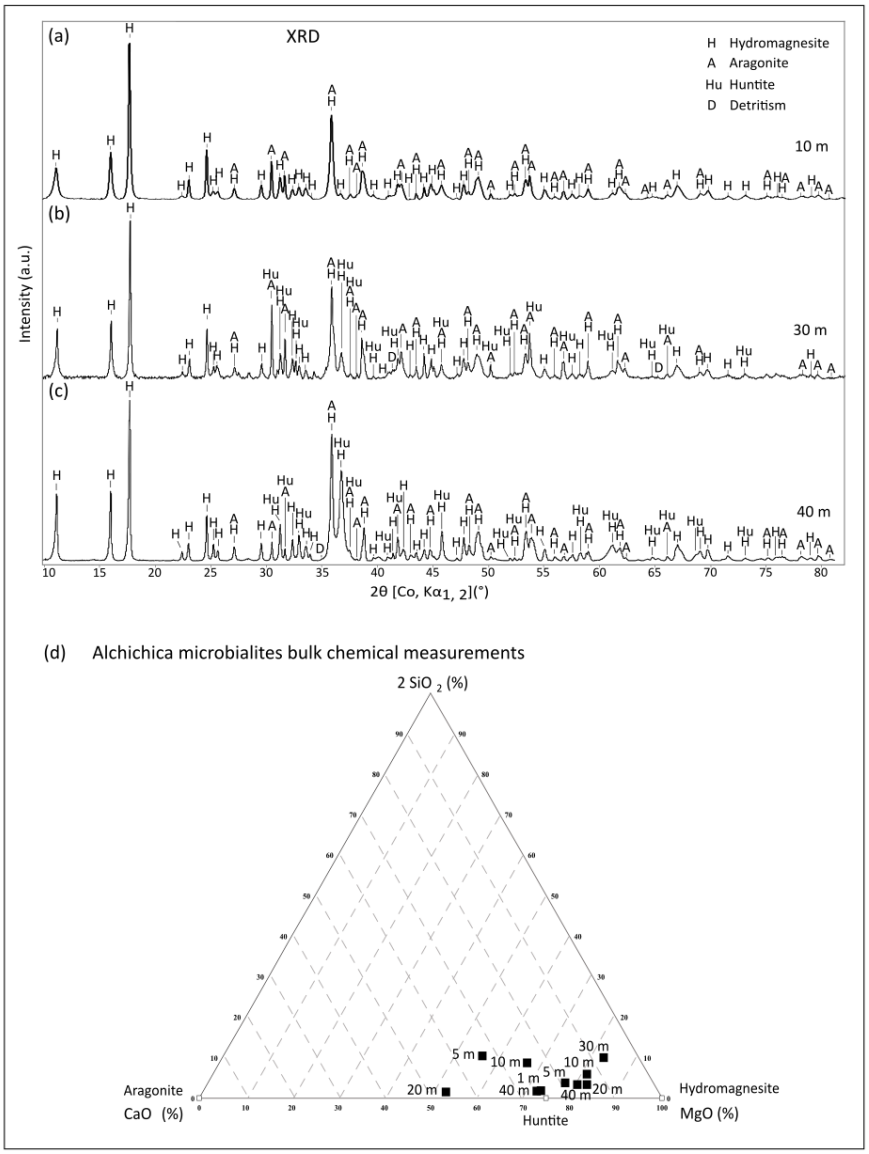

Figure S2: *Powder X-ray diffraction patterns and bulk chemical composition of Alchichica microbialites. Hydromagnesite (H), aragonite (A), huntite (Hu), LDH and detrital mineral phases (D) such as albite, anorthite and/or pyroxene were detected in these samples. (A) Powder X-ray diffraction pattern of a 10-m-deep microbialite sample; (B) Powder X-ray diffraction pattern of a 30-m-deep microbialite sample; (C) Powder X-ray diffraction pattern of a 40-m-deep microbialite sample; (D) Plot of the bulk chemical compositions of microbialites sampled in Lake Alchichica between 0 and 40 m in depth in May 2019 and October 2022 in a Mg-Ca-2*Si ternary diagram. The small empty squares represent the stoichiometries of hydromagnesite, huntite and aragonite. The figure is modified after Caumartin et al. (2025).*

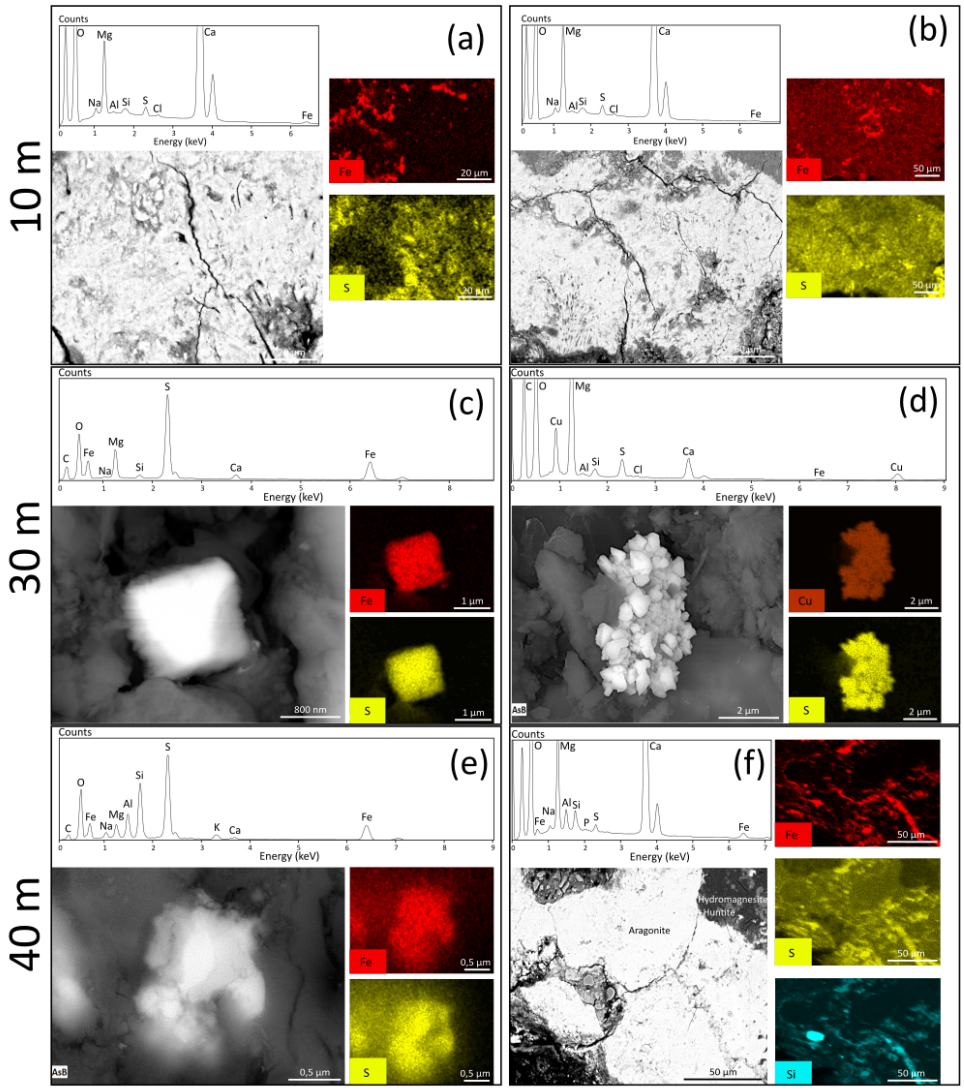

Figure S3: *Sulfur-bearing mineral phases in Lake Alchichica microbialites collected in October 2022 detected by SEM-EDXS. (a) SEM image in the BSE mode of an aragonitic surface layer in the 10-m-deep microbialite sample, with associated EDXS spectrum and elemental EDXS maps of iron (red) and sulfur (yellow); (b) SEM image in the BSE mode of another aragonitic surface layer of the 10-m-deep microbialite sample, with associated EDXS spectrum and elemental EDXS maps of iron (red) and sulfur (yellow); (c) SEM image in the BSE mode of euhedral crystal of iron sulfide on the 30-m-deep microbialite sample, with associated EDXS spectrum and elemental EDXS maps of iron (red) and sulfur (yellow); (d) SEM image in the BSE mode of a Cu-S precipitation in the 30-m-deep microbialite sample, with associated EDXS spectrum and elemental EDXS maps of copper (brown) and sulfur (yellow); (e) SEM image in the BSE mode of an iron sulfide precipitation in the 40-m-deep microbialite sample, with associated EDXS spectrum and elemental EDXS maps of iron (red) and sulfur (yellow); (f) SEM image in the BSE mode of an aragonitic surface layer of the 40-m-deep microbialite sample, with associated EDXS spectrum and elemental EDXS maps of iron (red), sulfur (yellow) and silica (blue).*

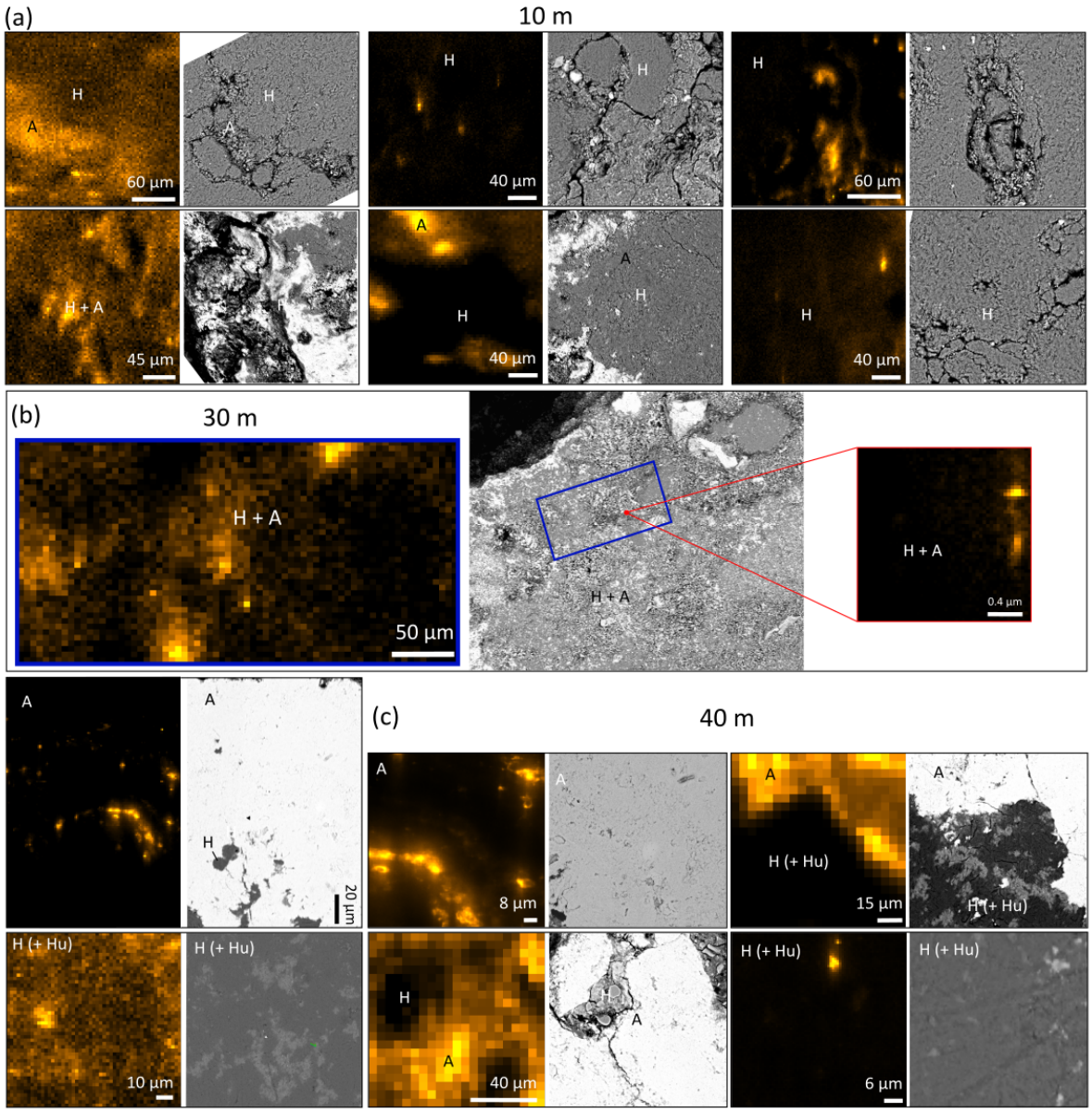

***Figure S4**: SR-µXRF sulfur maps acquired at the ID21 beamline on the Lake Alchichica microbialites collected in October 2022, associated with their SEM image in BSE mode (AsB). The following abbreviations are used: hydromagnesite (H), aragonite (A) and huntite (Hu). (a) SR-µXRF sulfur maps and corresponding SEM image in AsB mode acquired on the 10-m-deep microbialite thick section; (b) SR-µXRF sulfur maps and corresponding SEM image in AsB mode acquired on the 30-m-deep microbialite thick section. The SR-µXRF map surrounded by a blue line corresponds to the blue rectangle in the SEM image, the SR-µXRF map surrounded by a red line corresponds to the red dot in the SEM image; (c) SR-µXRF sulfur maps and corresponding SEM image in AsB mode acquired on the 40-m-deep microbialite thick section*

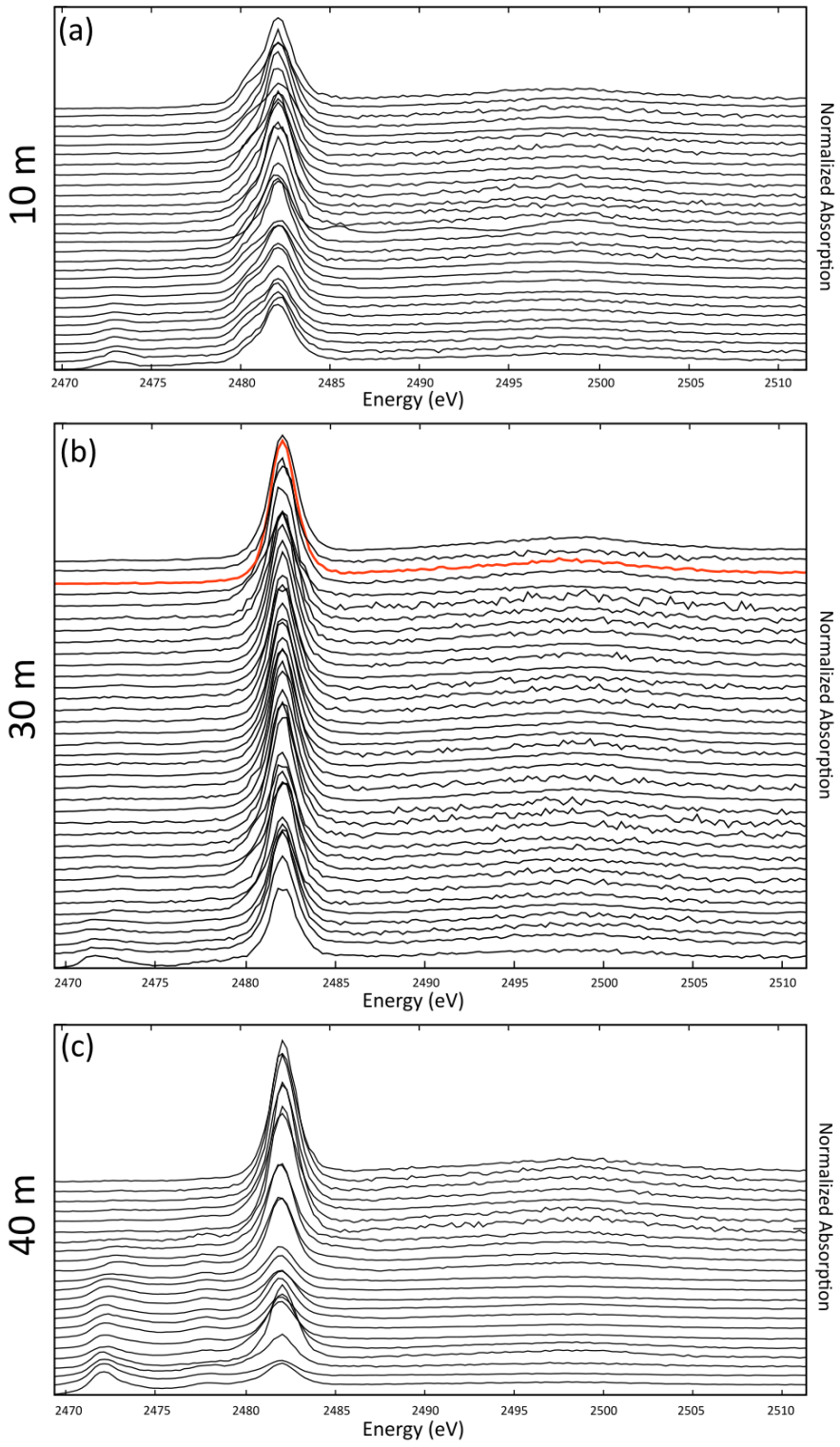

Figure S5: *Sulfur K-edge XANES spectra acquired on the Lake Alchichica microbialites collected in October 2022. (a) Sulfur K-edge XANES spectra acquired on the 10-m-deep microbialite thick section; (b) Sulfur K-edge XANES spectra acquired on the 30-m-deep microbialite thick section with in red the spectrum used as internal reference; (c) Sulfur K-edge XANES spectra acquired on the 40-m-deep microbialite thick section.*

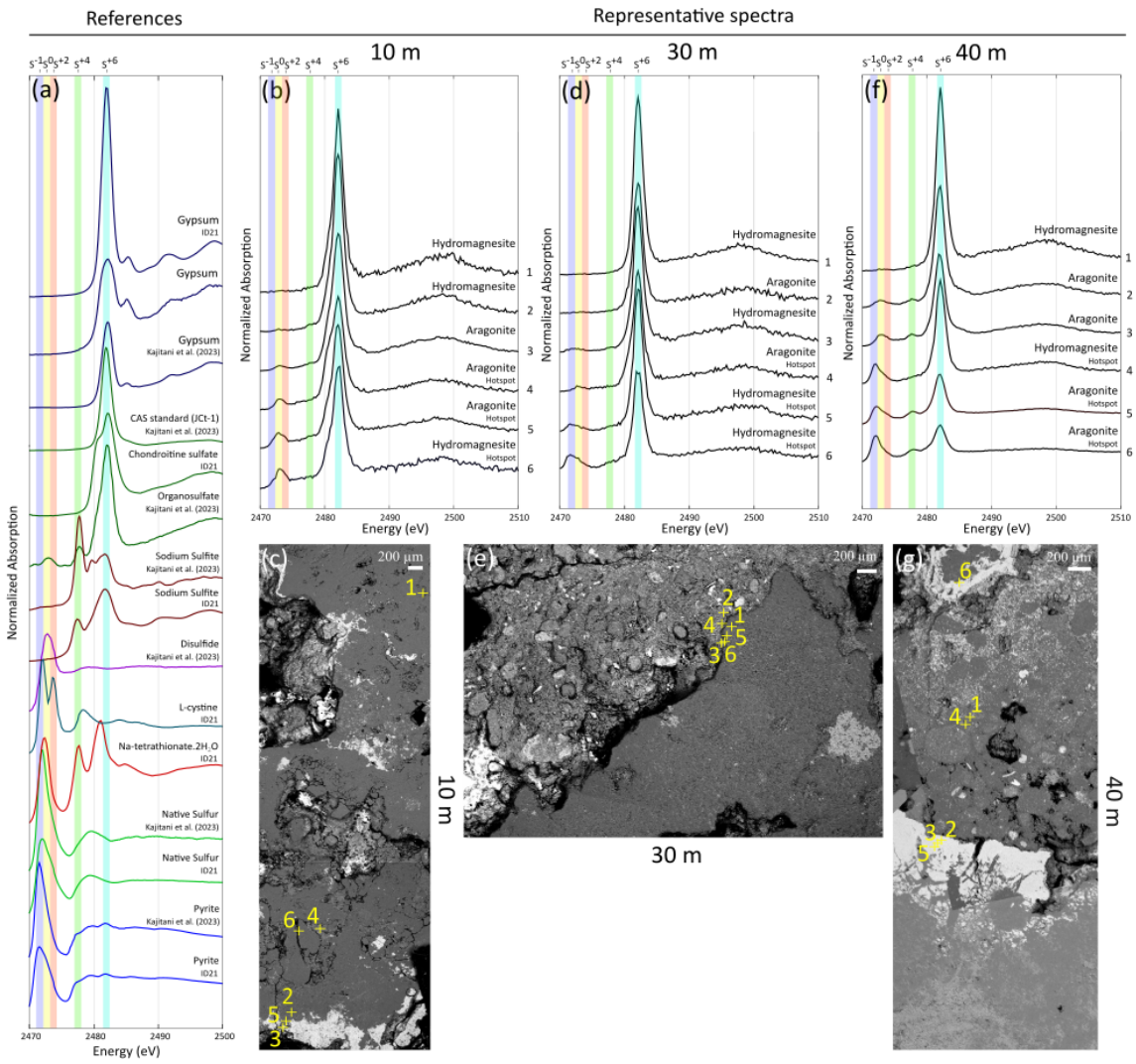

Figure S6: *Overview of the sulfur K-edge XANES spectra of the Lake Alchichica microbialites collected in October 2022 shown together with a list of reference sulfur XANES spectra from the ID21 organic and inorganic databases and the literature. (a) List of reference sulfur XANES spectra used to compare the microbialites sulfur XANES spectra (ID21 organic and inorganic databases; Kajitani et al., 2023); (b) Six numbered sulfur XANES spectra representatives of the dataset obtained for different mineral phases present in the 10-m-deep sample; (c) SEM image in the backscattered electron mode at large scale of the 10-m-deep sample. Numbered crosses indicate the places where corresponding numbered sulfur XANES spectra of the image b were acquired; (d) Six numbered sulfur XANES spectra representatives of the dataset obtained for different mineral phases present in the 30-m-deep sample; (e) SEM image in the backscattered electron mode at large scale of the 30-m-deep sample. Numbered crosses indicate the places where corresponding numbered sulfur XANES spectra of the image d were acquired; (f) Six numbered sulfur XANES spectra representatives of the dataset obtained for different mineral phases present in the 40-m-deep sample; (g) SEM image in the backscattered electron mode at large scale of the 40-m-deep sample. Numbered crosses indicate the places where corresponding numbered sulfur XANES spectra of the image f were acquired.*

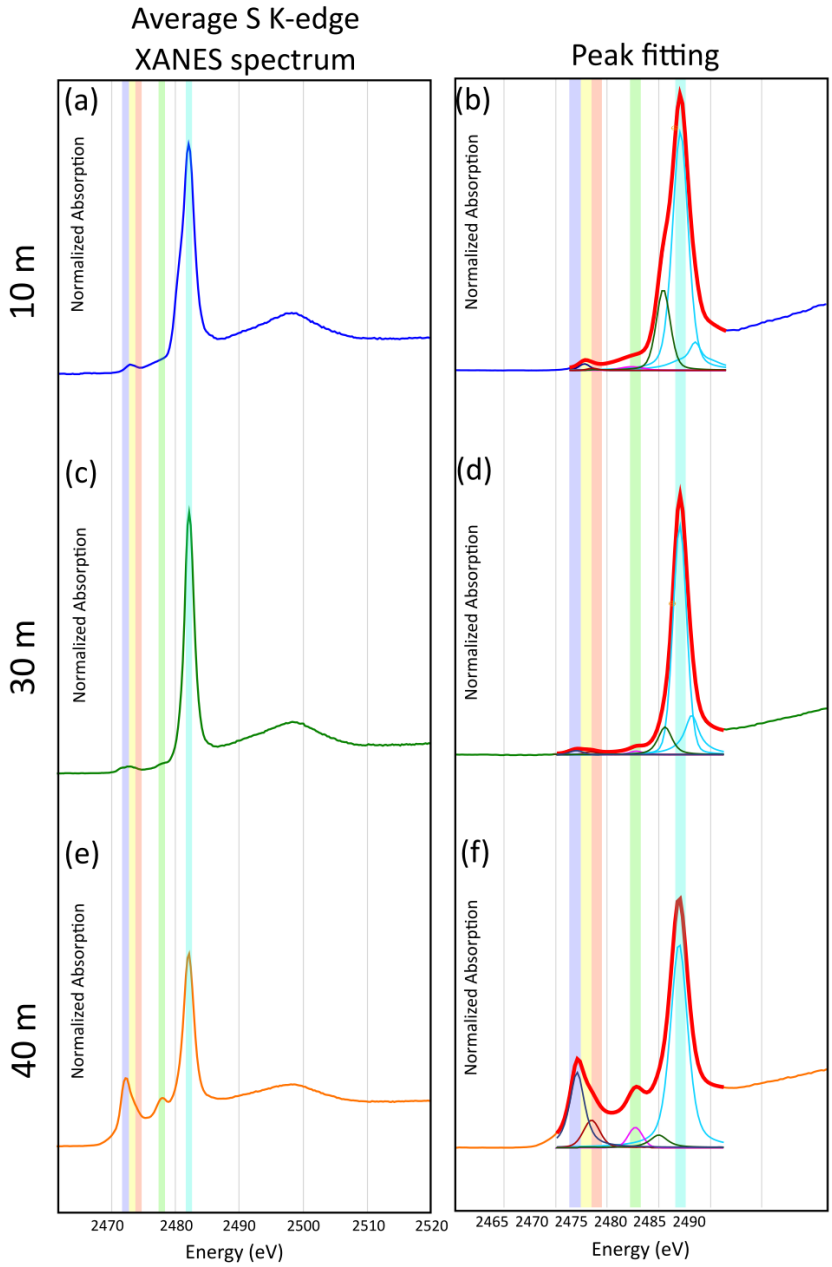

Figure S7: *Sulfur K-edge XANES spectra deconvolution. Oxidation states of the sulfur which were attributed to energy ranges are highlighted by different lines in dark blue for S(-I), yellow for S^0, red for organic S(-I) to S(0.5), green for S(II), and light blue for S(VI). On the right of the figure, the red line corresponds to the result of the spectrum deconvolution. The pseudo-Voigt curves used to fit the spectrum are represented under the spectrum. (a) Average sulfur K-edge XANES spectrum of the 10-m-deep sample; (b) Peak fitting result of the 10-m-deep average sulfur K-edge XANES spectrum; (c) Average sulfur K-edge XANES spectrum of the 30-m-deep sample; (d) Peak fitting result of the 30-m-deep average sulfur K-edge XANES spectrum; (e) Average sulfur K-edge XANES spectrum of the 40-m-deep sample; (f) Peak fitting result of the 40-m-deep average sulfur K-edge XANES spectrum.*

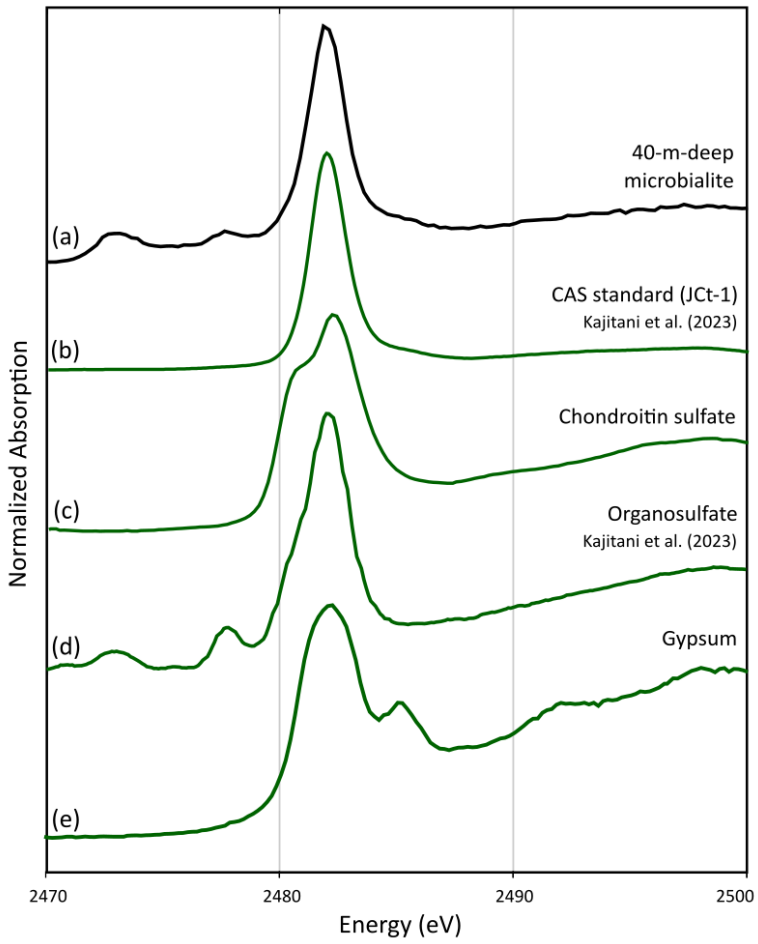

Figure S8: *Comparison of the sulfur K-edge XANES spectrum of a 40m-deep microbialite from Lake Alchichica (October 2022) with reference spectra for SO_4^{2-}. (a) Representative sulfur K-edge XANES spectrum of the 40-m-deep sample; (b) Reference sulfur K-edge spectrum of a CAS standard (JCt-1) from Kajitani et al., (2023); (c) Reference sulfur K-edge spectrum of a chondroitin SO_4^{2-} standard from the ID21 organic sulfur compounds database; (d) Reference sulfur K-edge spectrum of an organosulfate from Kajitani et al. (2023); (e) Reference sulfur K-edge spectrum of gypsum used as a standard during the beamtime at ID21.*

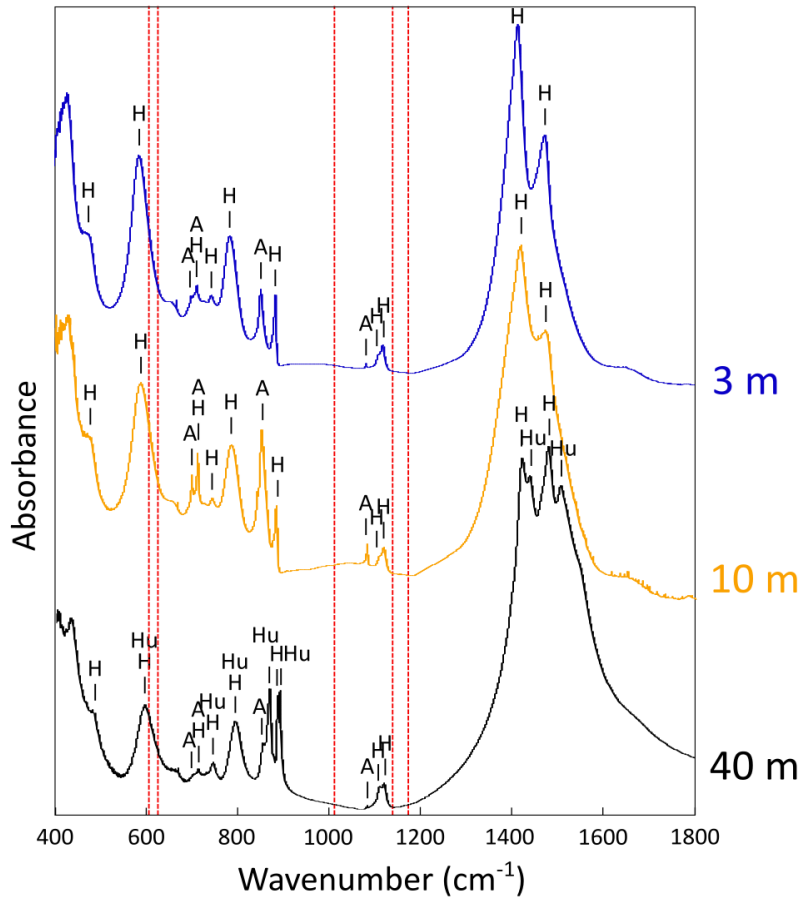

Figure S9: *FTIR spectra of Alchichica microbialites from different depths sampled in 2019 or 2022. The red dotted lines represent the bands characteristic of CAS (Balan et al., 2017; Floquet et al., 2015). The figure is modified after Caumartin et al. (2025).*

Supplementary References

Balan, E., Aufort, J., Pouillé, S., Dabos, M., Blanchard, M., Lazzeri, M., Rollion-Bard, C. and Blamart, D., 2017. Infrared spectroscopic study of sulfate-bearing calcite from deep-sea bamboo coral. European Journal of Mineralogy, 29(3), pp.397-408. https://doi.org/10.1127/ejm/2017/0029-2611

Floquet, N., Vielzeuf, D., Ferry, D., Ricolleau, A., Heresanu, V., Perrin, J., Laporte, D. and Fitch, A.N., 2015. Thermally induced modifications and phase transformations of red coral Mg-calcite skeletons from infrared spectroscopy and high-resolution synchrotron powder diffraction analyses. Crystal Growth & Design, 15(8), pp.3690-3706. https://doi.org/10.1021/acs.cgd.5b00291